# Investigation of Microcolumnar Scintillators on an Optical Fiber Coupled Compact Imaging System

Martin P. Tornai, *Member, IEEE*, Caryl N. Archer, Andrew G. Weisenberger, Randolph Wojcik, Vladimir Popov, Stan Majewski, Cynthia E. Keppel, Craig S. Levin, *Member, IEEE*, Sameer V. Tipnis, and Vivek V. Nagarkar

***Abstract*—A compact imaging system with a novel front-end detector is under investigation and development. Unique aspects of this collimatorless system include the use of thin arrays of many thousands of microcolumnar ($<$10 $\mu$m diameter) CsI front-end scintillators that are coupled through a four-times reducing fiber-optic (FO) bundle to a metal-channel multianode position sensitive photodetector. The tested arrays are 140 or 200 $\mu$m tall on faceplates of plane glass, FO, and FO with statistical extramural absorbers (EMAs). The highly discrete nature of the scintillator microcolumn arrays ensures very fine intrinsic spatial resolution, limited by the particle penetration and backscatter in the detector assembly. Their retro-reflector-tipped front ends facilitate light propagation toward the photodetector, ensuring good light collection. Monte Carlo simulations confirmed the limiting nature of beta particle penetration on measurable resolution. With this system, absolute light output was higher for the taller arrays, which indicates that these sizes are below the optimum for light output and energy absorption from the energetic beta particles; even taller scintillators, however, would suffer from increased backgrounds from annihilation radiation with positron detection. While MTF measurements with an X-ray source and microslit indicate the best response with the arrays on FO + EMA substrates, measurements with high and medium (1.7 MeV and 635 keV) energy beta line sources yield the best responses with the plane glass substrate, indicating that energy thresholding affects resolution in the classical way, even with these highly miniaturized arrays. Experiments with complex positron emission distributions along with large gamma-ray backgrounds, as may be expected during surgery, yield images with small background contamination and no distortions.**

***Index Terms*—Beta-ray detectors, biomedical nuclear imaging, nuclear imaging, optical fiber coupling, optical fibers, positrons, positron sensitive particle detectors, scintillation detectors.**

Manuscript received November 20, 2000. This paper was first presented at the IEEE Nuclear Science Symposium and Medical Imaging Conference, Lyon, France, October 15–20, 2000. This work was supported by NSF/MRI under Grant BES-9871378, by the Whitaker Foundation under Grant RG-99-0305, and by NIH under Grant RO1-CA76006.

M. P. Tornai and C. N. Archer are with the Section of Nuclear Medicine, Department of Radiology, Duke University Medical Center and the Department of Biomedical Engineering, Duke University, NC 27710 USA (e-mail: martin.tornai@duke.edu).

A. G. Weisenberger, R. Wojcik, V. Popov, and S. Majewski are with the Detector Group, Thomas Jefferson National Accelerator Facility, Newport News, VA 23606 USA.

C. E. Keppel is with the Physics Division, Thomas Jefferson National Accelerator Facility, Newport News, VA 23606 USA, and the Department of Nuclear and High Energy Physics, Hampton University, Hampton, VA 23668 USA.

C. S. Levin is with the Department. of Radiology, University of California at San Diego and VA Medical Centers, San Diego, CA 92161 USA.

S. V. Tipnis and V. V. Nagarkar are with Radiation Monitoring Devices, Inc. Watertown, MA 02172 USA.

Publisher Item Identifier S 0018-9499(01)05066-3.

## I. Introduction

NUCLEAR-medicine-based surgical guidance with nonimaging detector probes is gaining in acceptance and popularity [1]. One drawback of nonimaging guidance is the lack of ancillary information of the surveyed area, e.g., distinction between two neighboring radioactive regions, which can be more easily distinguished with an intraoperative imaging probe with very fine spatial resolution. More complete and accurate tumor resection has been shown to increase the lifespan and improve the quality of life of surgically treated patients. This has been an underlying motivation in the development of beta- and gamma-sensitive imaging as well as nonimaging detectors [1], with this class of intraoperative *imaging* detectors specifically designed to help delineate the postexcisional tumor boundaries, which a surgeon could subsequently identify and remove.

To date, positron emitting radiotracers (e.g., $^{18}F$-fluoro-deoxyuridine, $^{18}F$-FDG, and other compounds under development) whose annihilation gammas can be imaged with positron emission tomography (PET) promise an available means of intraoperatively imaging radiolabeled lesions and, specifically, their boundaries. Direct positron detection, however, with the accompanying 511-keV annihilation gamma backgrounds in the patient's body, has been shown to degrade image contrast [1].

Thus, a key aspect of this work, in contrast to earlier imaging work with lower-$Z$ scintillators [2]–[4] or semiconductors [1], [5], [6], is that considerably thinner, higher effective-$Z$ and higher density CsI scintillator plates are investigated here. The light output of CsI is markedly better than that of available lower-$Z$ scintillators, and individual elements could be uniformly discretized to repeatable micrometer sizes without the tedious process of cutting and polishing elements [7]–[10]. With these $<$10 $\mu$m discrete scintillator diameters possible, there is a very high degree of light channeling in the scintillator, in contrast to the light spreading and consequent resolution degradation seen with even very thin, continuous scintillator disks [3], [4].

These microcolumnar scintillators were originally developed for use with charge-coupled devices (CCDs) for low-energy digital X-ray imaging [8]–[10]. Taller ($\geq$100 $\mu$m) or larger ($>$10 $\mu$m diameter) microcolumns could be used for low-energy gamma-ray imaging with nuclear emission imaging techniques,

such as in compact gamma cameras and dedicated small area systems for specific applications. For example, some gamma camera systems under development with very high pixellation utilize 300-$\mu$m semiconductors [11] or similar sized pillars of cut and polished scintillators coupled to photodetectors [12]. These CsI microcolumnar arrays can be fabricated to these dimensions.

## II. Experimental Results

### A. CSDA and Monte Carlo Simulations

Thicknesses of the CsI scintillator plates intended for this application, sufficient to completely absorb positrons from $^{18}F$ ($E_{\max} = 635$ keV), were determined from continuous slowing down approximation (CSDA) calculations [13]. Both the particle range (integral pathlength) and the projected range (maximum distance from source origin) were determined since large thicknesses of the scintillation detector plates would likely increase the 511-keV annihilation gamma sensitivity. Due to the nature of direct *in situ* positron detection and imaging, annihilation gammas are prevalent in the background environment and are directly produced as a consequence of positron detection. This annihilation background has been previously shown to decrease image contrast [1]; hence detector thicknesses that correspond to the projected range of the intended particle provide high sensitivity for the charged particles but not for the resulting annihilation gammas.

Computer simulations, similar to those made for other scintillators and systems [3], [14], were performed to determine three-dimensional spatial distributions of $^{18}F$ positrons and $^{32}P$ ($E_{\max} = 1.71$ MeV) beta particle tracks in 0.1 mm up to 5-mm-thick CsI scintillators. The theoretical energy distributions were first calculated, and incident particle energies were sampled from that probability density function. To ensure that there were enough scatters between energy steps so that the multiple scatter formulas were satisfied for the many thousands of simulated particles, $^{18}F$ positrons were tallied in 3-keV steps, while $^{32}P$ betas were tallied in 5-keV steps. Although $dE$ was constant, $dE/dx$ for the given particle sampled from the energy distribution varied with energy, as the energy deposited increases while a particle slows down. The results of these simulations were compared with CSDA range and projected range calculations, which should yield significantly larger range values, given that these calculations do not account for the possibility of any single large collisional energy transfer (e.g., to produce delta-rays or *bremsstrahlung*) that is possible in the simulation.

### B. Microcolumnar Scintillators

Thousands of custom[1] vapor-deposited discrete microcolumnar CsI(Tl) scintillators ($Z_{\text{eff}} = 54$, $\rho = 4.5$ g/cm$^3$, $\lambda_{\max} = 540$ nm, $I = 54$k ph/MeV, $\tau = 900$ ns, $n = 1.78$) arranged in a disk as the front-end beta/positron sensitive detector were investigated (Fig. 1). The parameters of the investigated large scintillator arrays containing $\leq 10$ $\mu$m diameter microcolumnar scintillators are shown in Table I.

[1]RMD, Inc., Watertown, MA.

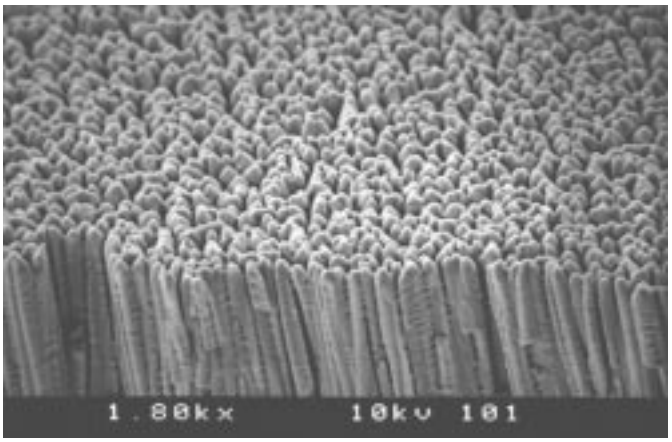


Fig. 1. Scanning electron micrograph of the top surface (particle incident side) of one microcolumnar CsI(Tl) array used in the imaging system. Note the regularity of the $<10$ $\mu$m diameter of each crystal as well as the conical retroreflector-like tips.

TABLE I
Physical Characteristics of the Microcolumnar Arrays

| Crystal Height ($\mu$m) | Array Dimensions (X x Y mm$^2$) | Substrate Material | Substrate Thickness (mm) |
|---|---|---|---|
| 140 | 25.4 $\phi$ | FO + EMA | 2.0 |
| 140 | 25.4 x 25.4 | FO | 1.0 |
| 140 | 25.4 x 25.4 | Plano Glass | 1.0 |
| 200 | 25.4 x 25.4 | FO + EMA | 2.0 |
| 200 | 25.4 x 25.4 | FO | 2.0 |
| 200 | 25.4 x 25.4 | Plano Glass | 1.0 |

The microcolumns are hermetically sealed with approximately 3–4 $\mu$m of sealant and an $\sim$0.2 $\mu$m layer of reflective aluminum on the source entrance front end, and are backed by available 1- to 2-mm-thick borosilicate fiber-optic (FO) or glass substrates. The elements in the FO substrate consist of 10-$\mu$m-diameter FOs with a numerical aperture (NA) of 0.66 and include a statistical extra mural absorber (EMA) that is used to absorb stray or scattered light that could spread through the FO array.

The conical peaks at the particle entrance ends (Fig. 1) act like retroreflectors [15], [16] and actually help to reflect scintillation light back down toward the photodetector, thus improving the light output of these tall yet narrow scintillators. Note that each column of CsI(Tl) is truly a distinct element with small air gaps that enhance total internal reflection along its side toward the substrate and photodetector.

Microcolumns of CsI(Na), an otherwise identical scintillator, whose emission spectrum ($\lambda_{\max} = 420$ nm) is better matched to the absorption of PMT photocathodes, have been developed elsewhere [7] and are also under investigation for more optimal spectral coupling.

### C. Fiber-Optic Tapered Coupling

The FO coupling and reducing bundle[2] is designed to extend the sensitive field of the position-sensitive (PS) PMT (Fig. 2).

[2]Schott Fiber Optic, Inc., Southbridge, MA.

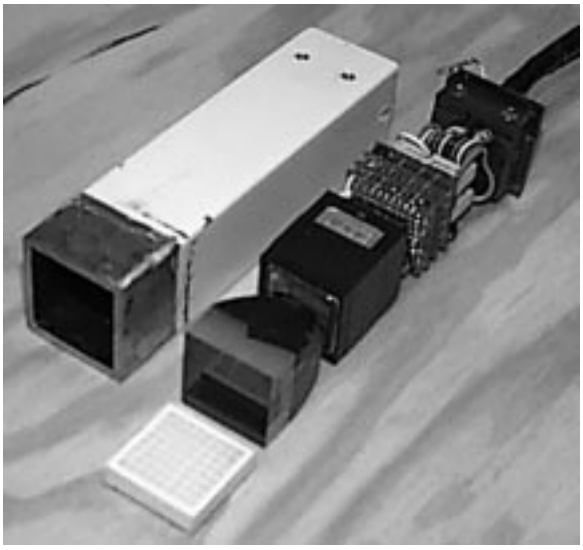

Fig. 2. Photograph of the components of the compact imaging system. The particular scintillator array shown (lower left) consists of an 8 × 8 array of 3-mm CsI(Tl) elements in white epoxy and was not one of those used in these experiments.

The FO taper is much larger in area than the tested scintillation arrays but is intended to match the array size in a final detector version. The FO bundle reduces the 9-cm$^2$ front surface in area by a factor of four and consists of 10-$\mu$m fibers, with 1.0 NA. The reducing FO also includes an EMA similar to that used with two of the scintillator assemblies.

Due to the 2.54-mm pixellated elements on the PSPMT (see Section II-D), an additional light diffuser was necessary to spread the light from the FO to multiple channels on the PSPMT. Testing of various thicknesses of acrylic light diffuser plates (1–10 mm) resulted in an optimal 3-mm-thick light diffuser with blackened sides as the most appropriate to ensure that enough parallel channels received a signal from which to calculate the position of beta interaction. This light diffuser provided good linearity and dynamic range across the resultant images.

### *D. PSPMT Electronics and Control*

The PSPMT[3] has 64 parallel channels, each 2.54 mm on a side, whose signals are divided by a custom-built resistive divider to reduce the number of output signals from 64 to 16 (eight each in $X$ and $Y$, respectively). The resistive divider acts to determine the center of gravity for the interactions in $X$ and $Y$ dimensions, which are further calculated in software on the list mode acquired data.

A discriminator signal is obtained by summing the 16 output signals above a noise threshold and then generating a delayed and amplified 1.5-$\mu$s gate with a custom NIM board to trigger the charge-sensitive FERA analog-to-digital converters.[4] All modules are under control by a G3 PowerPC Macintosh laptop computer running Kmax data acquisition software[5] through SCSI. Readout of the list mode collected data is similar to that in [17].

[3]Hamamatsu Corp., Tokyo, Japan, model R5900-M64.

[4]Lecroy Research Systems, Inc., Chestnut Ridge, NY.

[5]Sparrow Corp., Starkville, MI.

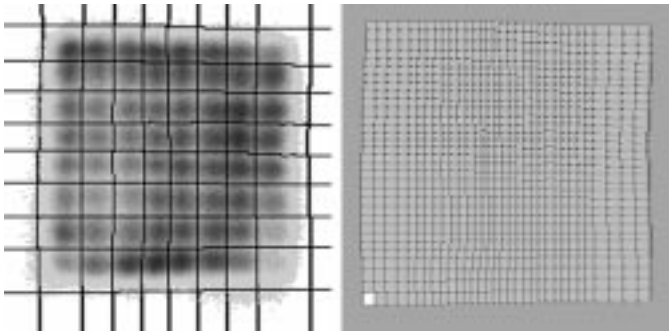

Fig. 3. (left) Linearity positioning map showing raw, uncorrected image of 8 × 8 array of 1.5-mm diameter transmission holes with results of two-dimensional valley finding algorithm, (right) further subdivided to yield 32 × 32 pixellation of the quantized lookup table. Measurement at left was with 140-$\mu$m-tall array on FO substrate.

### *E. Calibration and Image Display*

All calibrations, corrections, and display of image data were done in software programmed with Kmax in the Macintosh environment, as mentioned above. These are standard software-based NEMA-type calibrations used for gamma cameras that correct the list mode acquired data. A black plastic Delrin transmission mask with an 8 × 8 array of 1.5-mm holes spaced on twice their diameters was constructed. This mask was used to calibrate the linearity of the scintillator arrays in the imaging system (Fig. 3) and to use the discretization of the pseudocontinuous microcolumnar crystal arrays to obtain and incorporate uniformity and energy correction data on a regional basis. Note that it was impossible to identify any single microcolumn with this imaging setup, so this calibration procedure was established to regionally correct for variations across the scintillator surface; this is similar to the procedure used for continuous crystals in clinical gamma cameras. While a drawback of this approach was that we were limited to a 32 × 32 pixellated subdivision of the raw (~ 260 × 260 pixel) data, thus losing spatial resolution due to discretization effects, each element in the corrected 32 × 32 image arrays contained independent position and spectral information about that immediate region. Thus, this holospectral information in the data could be further exploited in an effort to optimize the imaging system.

### *F. Line Source and Phantom Measurements*

Intrinsic line spread functions (LSFs) were obtained for each scintillator array on an FO substrate by illuminating the arrays through a 10-$\mu$m tungsten slit with X-rays generated from a $W$ target.[6] Acquisition parameters include 40-kVp source energy, 1.25-s exposure, source distance of 45 cm, and a 3 : 1 FO taper on a CCD measurement system (Photometrix) that had 14-bit dynamic range. These LSFs were measured in the standard way for CCD calibration, and the modulation transfer functions (MTFs) were obtained as the Fourier transforms of the LSFs [18]. Extrinsic LSF measurements of emission line

[6]Gendex Corp., model GX1000.

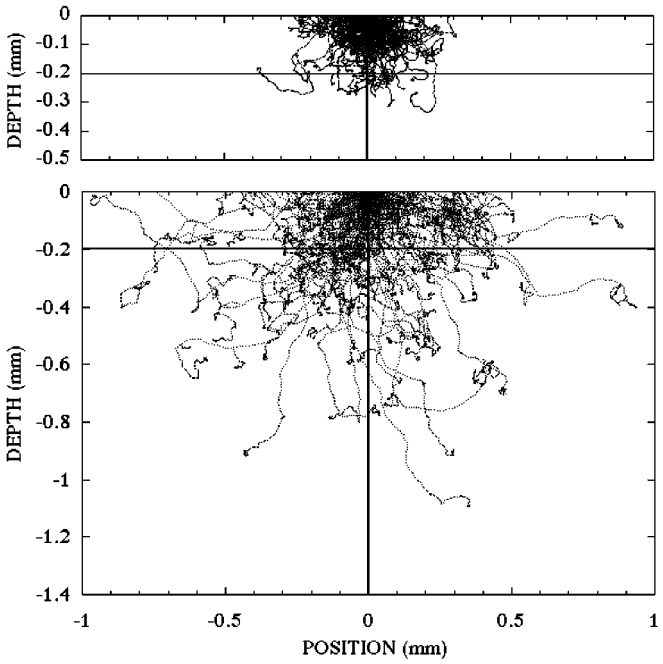


Fig. 4. Monte Carlo particle tracking simulation results for (top) $^{18}F$ and (bottom) $^{32}P$ in thick CsI media. In both cases, the horizontal line delineates the maximum thickness of CsI used here, and the vertical line approximately represents the width of a single microcolumnar scintillator. Source origin is at (0,0).

sources made of thread ($\ll$1 mm diameter) soaked in $\sim$925 kBq solutions of $^{32}P$ and $^{18}F$ and suspended in air with a custom-built C-clamp were acquired with the lines positioned horizontally and diagonally on the various crystal surfaces.

A custom-built 1-cm-thick acrylic transmission phantom[7] containing six sectors of holes (1.2, 1.5, 2.2, 3.0, 3.5, 4.0 mm diameters for each sector) with the center-to-center spacing on twice their diameters was imaged with $^{32}P$ betas with all scintillator combinations. Some holes in the 1.5- and 2.2-mm sectors of the transmission phantoms were partially filled with 222 and 181 kBq of $^{18}F$ activity in water, respectively, and sealed with one layer of clear tape. Emission images of these partially filled holes were obtained by themselves and also with 15 MBq of $^{18}F$ activity in 1.5 L of water directly behind the positron emission source simulating a source of annihilation contamination.

## III. Results

### A. Monte Carlo Particle Tracking

Results of the Monte Carlo simulations clearly demonstrate that the incident particles' penetration will play a more dominant role in spatial resolution degradation than the intrinsic 10 $\mu$m microscintillator size (Fig. 4). In comparison, CSDA range calculations yield a maximum range (complete pathlength) of 920 $\mu$m for $^{18}F$ positrons and a projected range (maximum distance attained from source) of 460 $\mu$m, while the simulation results indicate mean values much smaller than those calculated. Based on these particle tracking results, it might seem desirable to have scintillator thicknesses

[7]Data Spectrum Corp., Hillsborough, NC.

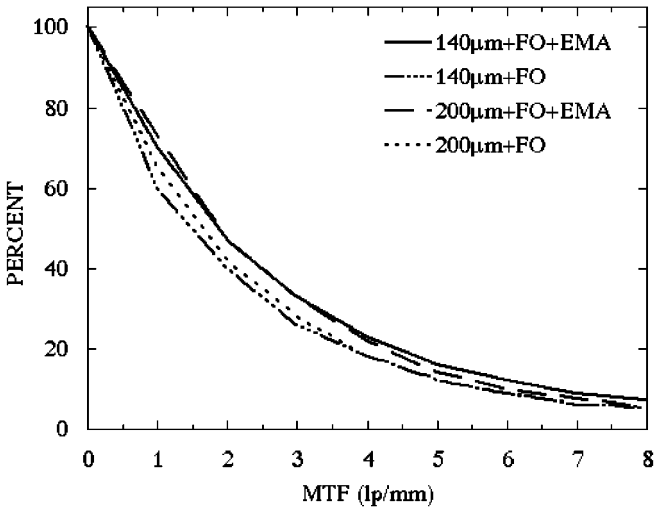


Fig. 5. MTF results for some scintillator arrays on two indicated substrates. The Nyquist frequency is 8.7 lp/mm.

of $\sim$400 $\mu$m to have a good efficiency for $^{18}F$ positrons. However, thicker beta detectors will be accompanied by larger annihilation backgrounds. Based on results of simulations and measurements of larger quantized CsI(Tl) scintillators [19], [20] and the consequent decreased light output expected with taller, narrower discrete elements, shorter elements in the arrays were initially tested (Table I).

### B. Intrinsic Spatial Resolution

The intrinsic MTFs of the measured arrays indicate that the shorter arrays with FO + EMA have a better frequency response than the other arrays (Fig. 5). This is not surprising given that there is less chance for light to spread, and hence decrease in spatial resolution, within normally irradiated shorter crystals on a substrate that partially absorbs stray light. All MTFs were quite similar, which also indicates that the highly discrete nature of the microcolumns plays a dominant role in determining the intrinsic response of the system. Note that the plano-glass substrate arrays measured with the transmission slit had LSFs with large tails that precluded adequate determination of the Fourier transforms of the LSFs.

Complex transmission distributions were imaged to empirically determine the ability to visualize juxtaposed regions of radioactivity (Fig. 6). The smallest discernible hole size was 1.5 mm with center-to-center spacing on twice that diameter, indicating that the intrinsic system resolution was better than 1.5 mm for the uncorrected data. Furthermore, one reason that the measured resolution is just $<$1.5 mm is due to the particle penetration through the detector along with backscatter from the FO taper immediately following it. The phenomenon has been observed previously [4]. While it is possible that there is only enough light generated in a bundle of microcrystals that is roughly 1.5 mm in diameter to yield a large enough signal that can be distinguished from neighboring regions, each microcrystal can more easily be read out when coupled to individual elements of a CCD. Of course, in that current-mode configuration, the ability for energy discrimination, in contrast to pulse counting techniques, is eliminated.

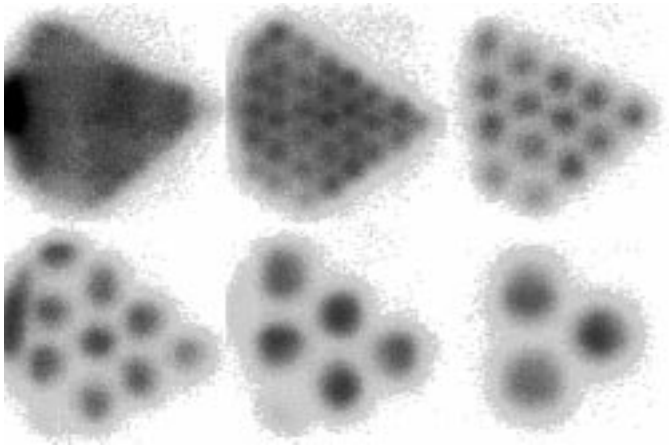

Fig. 6. (From left to right, upper to lower) Uncorrected raw images of $^{32}P$ transmission events through 1.2, 1.5, 2.2, 3.0, 3.5, and 4.0 mm holes spaced on twice their diameters for the 140 $\mu$m tall array on FO + EMA substrate.

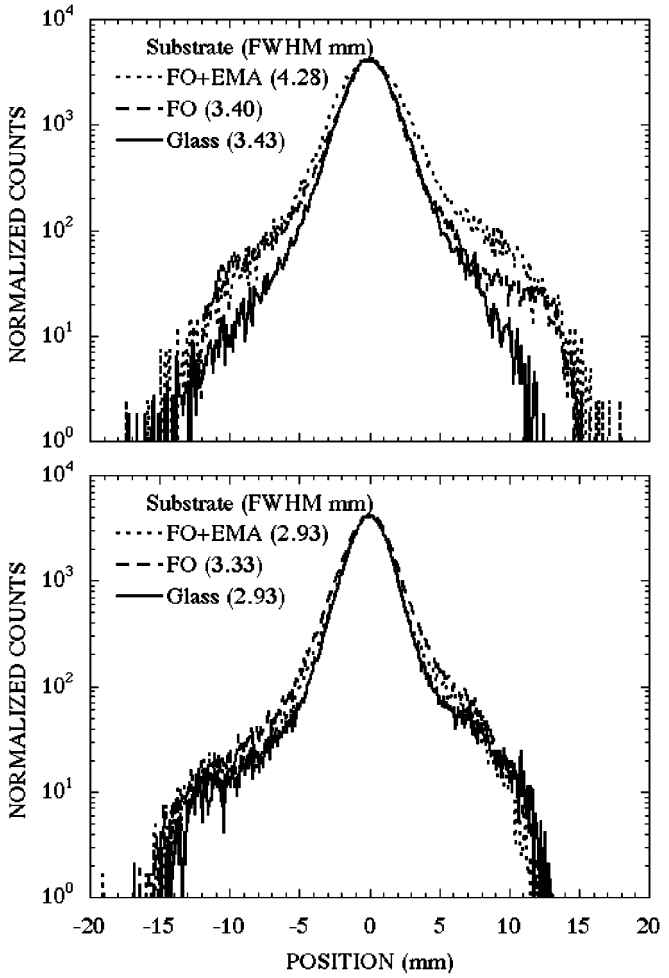


Fig. 7. Semi-log plots of uncorrected emission LSFs for all arrays measured with a horizontal $^{32}P$ line source in air, directly on top of the (top) 140-$\mu$m arrays and (bottom) 200-$\mu$m arrays. FWHMs listed in the key.

### C. Extrinsic Spatial Resolution

Extrinsic parameters measured with $^{32}P$ in the assembled imaging system yielded large full-widths at half-maxima (FWHM) for the exposed emission line source (Figs. 7 and 8), most likely due to the large particle penetration in the detector

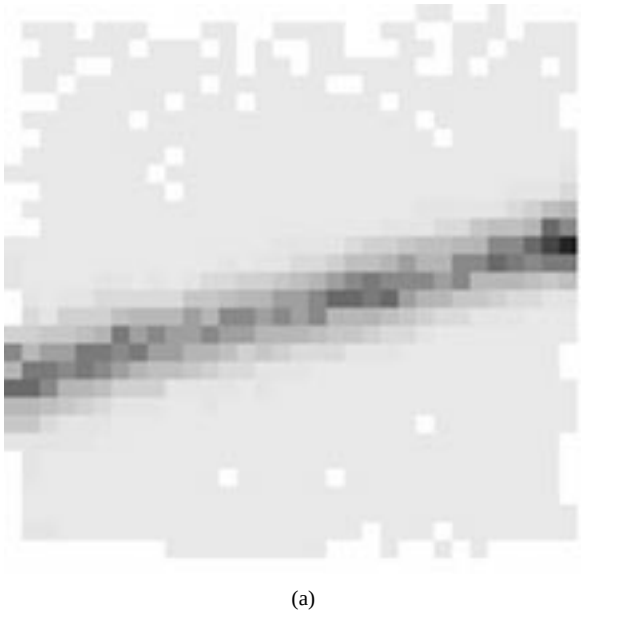

(a)

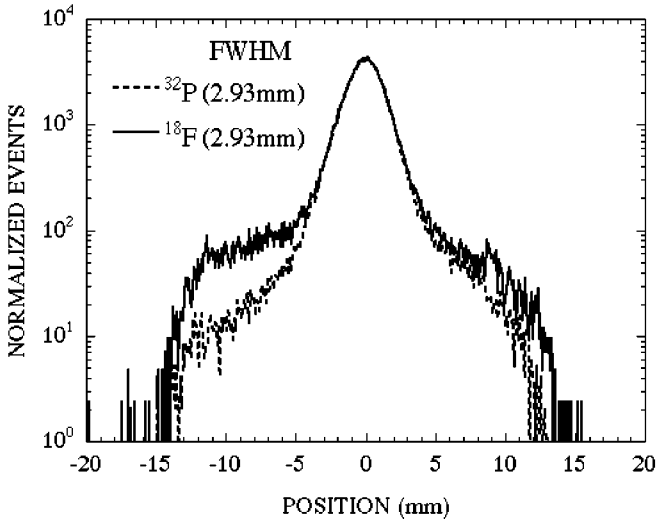


(b)

Fig. 8. LSF image and profiles of the 200-$\mu$m array on the glass substrate. (a) 32 × 32 corrected image (see Section III-C) of the exposed $^{18}F$ line source. (b) Superimposed, uncorrected LSFs of $^{18}F$ and $^{32}P$. Note high tails in the $^{18}F$ spectrum due to the presence of the annihilation background in the detector.

(Fig. 4, bottom) and backscatter of energetic particles a large distance away from the source.

There was an inverse trend in extrinsic spatial response to that of the intrinsic MTF measurements. That is, the arrays on substrates where higher light collection along with greater light spreading was expected (plano > FO > FO + EMA) yielded somewhat smaller measured FWHMs. This is consistent with the notion that spatial resolution is proportional to light intensity, since the intrinsic measurements utilized an integrating current detector without energy discrimination and the extrinsic measurements used a classical nuclear emission detector arrangement with PSPMT (see Section II-D).

Measurements of relative light output and signal-to-noise ratios (SNRs) confirmed the relative signal intensities of the different arrays on various substrates (Table II). The taller microcolumns were measured to have greater light output than

TABLE II
INTRINSIC MEASUREMENT RESULTS OF THE SCINTILLATOR ARRAYS

| Crystal Height (μm) | Substrate Material | Relative Light Output | SNR |
|---|---|---|---|
| 140 | FO + EMA | 0.34 | 143 |
| 140 | FO | 0.70 | 226 |
| 140 | Plano Glass | 0.70 | 245 |
| 200 | FO + EMA | 0.44 | 196 |
| 200 | FO | 1.00 | 325 |
| 200 | Plano Glass | 0.91 | 347 |

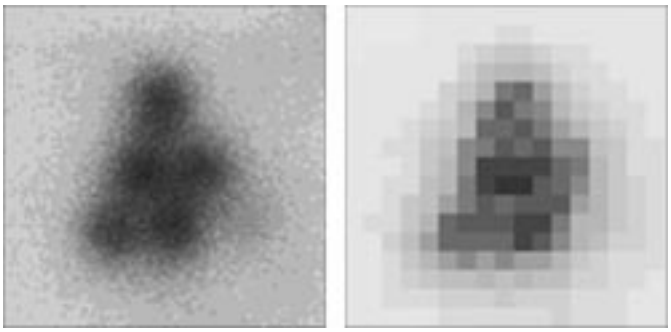

(a) (b)

Fig. 9. Cropped images of ~6 partially filled 1.5-mm holes on 3.0-mm centers with 222-kBq $^{18}F$ activity in (a) the raw uncorrected image and (b) the corrected image with 32 × 32 pixellation, measured with 200-$\mu$m-tall array on plano-glass substrate.

the shorter ones, which seemingly contradicts measurements of larger cross-section (>1 × 1 mm$^2$) quantized scintillators of various heights used for gamma-ray detection [19], [20].

While for arrays of a given height the light output result is consistent with the expected light absorption through the various substrates, the seemingly inverse relation of light output and height is an interesting result. One explanation is that the light output and detector efficiency are tied together [3], [21] and that there is more complete energy deposition in the taller detector, and hence a greater light output. This explanation is corroborated by previous measurements [3], [21] and also follows the results of [19], [20] if both detection efficiency and light collection are considered in the detected signal intensity.

### *D. Emission Imaging of Positron Distributions*

Images of complex positron emission distributions illustrate the resolution losses associated with $2\pi$ emissions directly on the detector surface (Fig. 9), as well as the contrast degradation due to presence of annihilation gamma backgrounds (Fig. 10). There was difficulty in discerning the 1.5-mm-diameter wells, but visualization of the 2.2-mm wells with emission imaging indicates that the emission resolution is still better than that measured with the LSFs.

The addition of the gamma-ray background immediately behind the positron emission source simulated expected clinical imaging conditions. While there is an apparent loss in spatial resolution, the signal degradation is probably more due to decreased image contrast. The difference image (Fig. 10) illustrates that the gamma ray contribution is fairly uniform over the detector surface, but also that there are focal spots that correspond to the locations of the emission sources. This is not surprising, since positron detection liberates annihilation gammas in efficient positron detectors.

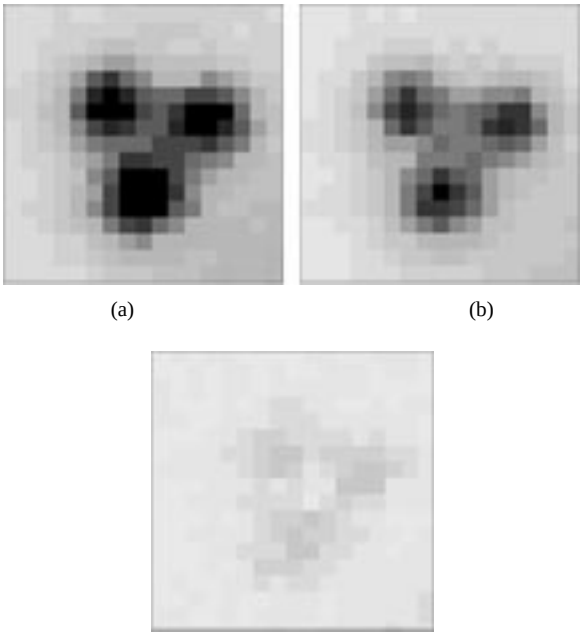

(a) (b)

(c)

Fig. 10. Cropped images of three partially filled 2.2-mm diameter holes on 4.4-mm centers, with 181 kBq of $^{18}F$ activity. (a) Emission holes with 15-MBq gamma-ray background. (b) Emission holes without any additional background. (c) Difference image illustrating spatial distribution of annihilation gamma-ray signal only. All images shown were with the 200-$\mu$m-tall array on plano-glass substrate.

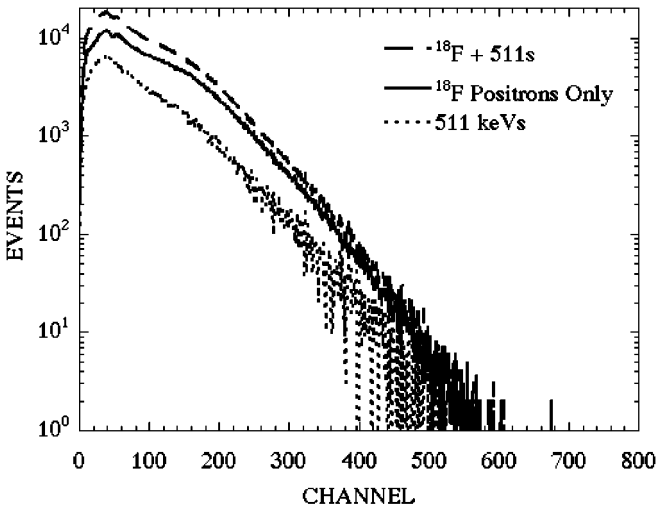


Fig. 11. Semi-log plots of energy spectra from the data in Fig. 10 illustrating beta + gamma spectra, beta-only spectra, and the difference spectra representing the gamma only signal.

Furthermore, the distinction between energy spectra without and with background contribution was small but significant (Fig. 11) as the 511-keV gamma-ray efficiency is low with different CsI(Tl) heights. The gamma-ray background contribution, measured as the ratio of integral counts of the total minus

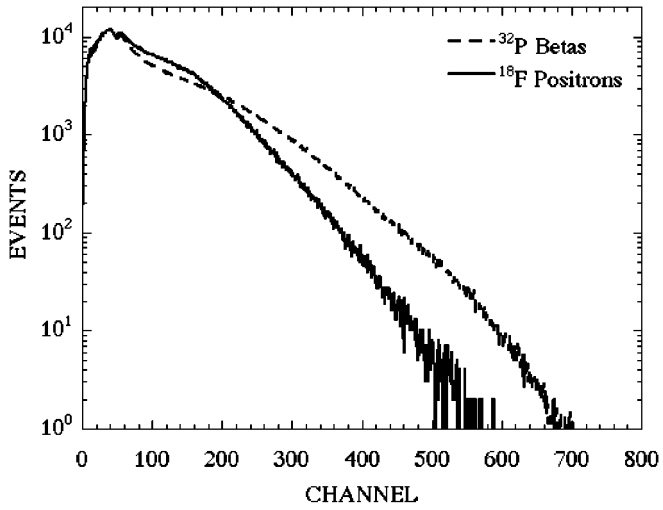


Fig. 12. Semi-log plots of energy spectra illustrating differences between $^{32}P$ higher energy beta emissions and lower energy $^{18}F$ positron spectra.

beta-only events to the total events in the spectra (Fig. 11) was 32% of the total signal. The shorter detectors also facilitate incomplete energy deposition due to inefficiency for Compton scattered photons as well as Compton electrons and photoelectrons that are not completely stopped in the scintillator.

However, the energy response of the scintillator arrays did distinguish between the lower and higher energy betas (Fig. 12). The light output was not proportional to the factor of 2.7 difference between incident particle endpoint energies. The primary reason for this is due to the incomplete energy deposition from the higher energy, near minimum ionizing particles. This effect does not result in degraded system sensitivity, since partial energy deposition from any single event greater than threshold is still a valid event, but it affects the overall pulse height. Note also that for these shorter scintillators and disparate incident particle energies, the higher endpoint energy particles will more uniformly deposit their energy along the length of the microcolumns, while the lower endpoint energy particles will predominantly deposit their energy nearer to the incident surface. This factor can also influence the total light output from these tall and very narrow scintillators.

## IV. Conclusion

A novel, compact imaging system was described that employs thousands of $<$10-$\mu$m-diameter microcolumnar CsI(Tl) scintillators with FO coupling to the position sensitive PMT. The intrinsic (MTF) and extrinsic spatial responses were determined and found to be dependent on the overall energy response of the incident particle, and also ultimately limited by the beta particle penetration rather than the intrinsic detector size. Monte Carlo particle tracking simulations confirmed the limiting effects on spatial resolution. With the best 200-$\mu$m scintillator array on the plano-glass substrate, the LSFs of particles of disparate energies, including additional annihilation backgrounds, were equivalent. The tails of the LSFs were higher in the positron measurements due to the presence of annihilation backgrounds.

Images of complex transmission phantoms indicate that the system resolution is $<$1.5 mm. This indicates that the 200-$\mu$m thin, high effective-$Z$, high-density scintillator would be an effective and efficient beta detector for various incident particles. Furthermore, emission images of complex distributions were clearly discernible and very sensitive to small quantities of $^{18}F$ activity. While the accompanying annihilation background degraded image contrast, the overall 511-keV backgrounds had an $\sim$30% contribution to the energy spectrum, and pulse-height differences were clearly discriminated between particles of various endpoint energies. One very interesting result of these measurements of ultra-narrow and tall microcolumnar scintillators was that for the sizes measured, the taller scintillators had higher light output and yielded better SNRs than the shorter scintillators. This fact indicates that the tradeoff between detection efficiency and light output as a function of thickness is still below the peak light output for these scintillator heights. While light output may still increase with thicker arrays of microcolumns, this is offset by the fact that gamma-ray background contributions would also continue to increase with taller scintillators.

## Acknowledgment

The authors would like to thank the Duke University Medical Center Radiopharmacy and PET Cyclotron for providing the isotopes used in this study; and the Department of Radiology in the Durham Veterans Administration Hospital for providing facilities where the experiments were performed.

## References

[1] E. J. Hoffman, M. P. Tornai, M. Janecek, B. E. Patt, and J. S. Iwanczyk, "Intraoperative probes and imaging probes," *Eur. J. Nucl. Med.*, vol. 26, no. 8, pp. 913–935, 1999.

[2] L. R. MacDonald, M. P. Tornai, C. S. Levin, J. Park, M. Atac, D. B. Cline, and E. J. Hoffman, "Investigation of the physical aspects of beta imaging probes using scintillating fibers and visible light photon counters," *IEEE Trans. Nucl. Sci.*, vol. 42, pp. 1351–1360, Aug. 1995.

[3] C. S. Levin, L. R. MacDonald, M. P. Tornai, E. J. Hoffman, and J. Park, "Optimizing light collection from thin scintillators used in a beta-ray camera for surgical use," *IEEE Trans. Nucl. Sci.*, vol. 43, pp. 2053–2060, June 1996.

[4] M. P. Tornai, L. R. MacDonald, C. S. Levin, S. Siegel, and E. J. Hoffman, "Design considerations and initial performance of a 1.2 cm$^2$ beta imaging intra-operative probe," *IEEE Trans. Nucl. Sci.*, vol. 43, pp. 2326–2335, Aug. 1996.

[5] M. P. Tornai, B. E. Patt, J. S. Iwanczyk, C. R. Tull, L. R. MacDonald, and E. J. Hoffman, "A novel silicon array for intraoperative charged-particle imaging," in 1998 IEEE NSS/MIC, Toronto, Canada, Nov. 8–14, 1998.

[6] D. Visvikis and J. H. MacDonald, "A solid state detector for intraoperative imaging," *IEEE Trans. Nucl. Sci.*, vol. 46, pp. 1172–1176, 1999.

[7] M. Ito, M. Yamaguchi, and K. Oba, "CsI(Na) scintillation plate with high spatial resolution," *IEEE Trans. Nucl. Sci.*, vol. NS-34, pp. 401–405, Feb. 1987.

[8] V. V. Nagarkar, T. K. Gupta, S. R. Miller, Y. Klugerman, M. R. Squillante, and G. Entine, "Structured CsI(Tl) scintillators for x-ray imaging applications," *IEEE Trans. Nucl. Sci.*, vol. 45, pp. 492–496, June 1998.

[9] V. V. Nagarkar, S. V. Tipnis, T. K. Gupta, S. R. Miller, V. B. Gaysinskiy, Y. Klugerman, M. R. Squillante, G. Entine, and W. W. Moses, "High speed x-ray imaging camera using a structured CsI(Tl) scintillator," *IEEE Trans. Nucl. Sci.*, vol. 46, pp. 232–236, June 1999.

[10] S. V. Tipnis, V. V. Nagarkar, V. B. Gaysinskiy, P. O'Dougherty, Y. Klugerman, S. R. Miller, and G. Entine, "Large area CCD based imaging system for mammography," in *1999 IEEE NSS/MIC Conf. Rec.*, 1999.

[11] G. K. Kastis, H. B. Barber, and H. H. Barrett *et al.*, "High resolution SPECT imager for three-dimensional imaging of small animals," *J. Nucl. Med.*, vol. 39, no. 5, p. 9P.

[12] R. Pani, F. de Notaristefani, K. Blazek, P. Maly, R. Pellegrini, A. Pergola, A. Soluri, and F. Scopinaro, "Multi-crystal YAP:Ce detector system for position sensitive measurements," *Nucl. Instrum. Meth.*, vol. A348, no. 2–3, pp. 551–558, 1994.

[13] NIST"CSDA range tables,", http://physics.nist.gov/PhysRefData/Star.

[14] C. S. Levin and E. J. Hoffman, "Calculation of positron range and its effect on the fundamental limit of positron emission tomography system spatial resolution," *Phys. Med. Biol.*, vol. 44, no. 3, pp. 781–799, 1999.

[15] J. S. Karp and G. Muehllehner, "Performance of a position-sensitive scintillation detector," *Phys. Med. Biol.*, vol. 30, no. 7, pp. 643–655.

[16] J. Strobel, N. H. Clinthorne, and W. L. Rogers, "Design studies for a cesium iodide silicon photodiode gamma camera," *J. Nucl. Med.*, vol. 38, no. 5, pp. 31P–32P.

[17] S. Avery, C. Keppel, S. Majewski, A. G. Weisenberger, R. Wojcik, and C. Zorn, "Small gamma imaging probe with millimeter spatial resolution," in *1997 IEEE NSS/MIC Conf. Rec.*.

[18] H. Fujita, T. Du-Yih, I. Takumi, D. Kunio, M. Junji, U. Katsuhiko, and O. Akiyoshi, "A simple method for determining the modulation transfer function in digital radiography," *IEEE Trans. Med. Imag.*, vol. 11, no. 1, pp. 34–39, 1992.

[19] A. J. Bird, T. Carter, A. J. Dean, D. Ramsden, and B. M. Swinyard, "The optimization of small CsI(Tl) gamma-ray detectors," *IEEE Trans. Nucl. Sci.*, vol. 40, pp. 395–399, Aug. 1993.

[20] M. P. Tornai, C. S. Levin, L. R. MacDonald, and E. J. Hoffman, "Investigation of crystal geometries for fiber coupled gamma imaging intra-operative probes," *IEEE Trans. Nucl. Sci.*, vol. 44, pp. 1254–1261, June 1997.

[21] M. P. Tornai, E. J. Hoffman, L. R. MacDonald, and C. S. Levin, "Characterization of fluor concentration and geometry in organic scintillators for *in situ* beta imaging," *IEEE Trans. Nucl. Sci.*, vol. 43, pp. 3342–3347, Dec. 1996.